



# The effect of stress triaxiality on the phase transformation in transformation induced plasticity steels: Experimental investigation and modelling the transformation kinetics

E. Polatidis<sup>a,\*</sup>, G.N. Haidemenopoulos<sup>b</sup>, D. Krizan<sup>c</sup>, N. Aravas<sup>b,d</sup>, T. Panzner<sup>a,e</sup>, M. Šmíd<sup>f</sup>, I. Papadioti<sup>b</sup>, N. Casati<sup>f</sup>, S. Van Petegem<sup>f</sup>, H. Van Swygenhoven<sup>f,g</sup>

<sup>a</sup> Laboratory for Neutron Scattering and Imaging, Paul Scherrer Institute, CH-5232, Villigen PSI, Switzerland

<sup>b</sup> Department of Mechanical Engineering, University of Thessaly, 26504, Volos, Greece

<sup>c</sup> Research and Development Department, Business Unit Coil Voestalpine Stahl GmbH, 4020, Linz, Austria

<sup>d</sup> International Institute for Carbon Neutral Energy Research (WPI-I2CNER), Kyushu University, 744 Moto-oka, Nishi-ku, Fukuoka, 819-0395, Japan

<sup>e</sup> Swissneutronics AG, CH-5313, Klingnau, Switzerland

<sup>f</sup> Swiss Light Source, Paul Scherrer Institute, CH-5232 Villigen PSI, Switzerland

<sup>g</sup> Neutrons and X-rays for Mechanics of Materials, IMX, École Polytechnique Fédérale de Lausanne, CH-1015, Lausanne, Switzerland

## ARTICLE INFO

### Keywords:

TRIP  
Steel  
Martensite  
Kinetics  
Model

## ABSTRACT

In situ multiaxial loading during neutron diffraction tests were undertaken on a low-alloyed Quenched and Partitioning (Q&P) Transformation Induced Plasticity (TRIP) Bainitic Ferrite (TBF) steel with dispersed austenite particles. The effect of stress triaxiality on the evolution of the deformation-induced martensite is investigated under uniaxial- and equibiaxial-tension as well as tension/compression with a ratio of  $-1:6$ . It is shown that transformation is not a monotonic function of stress triaxiality; the amount of deformation-induced martensite is similar under uniaxial and equibiaxial tension but it is significantly smaller under tension/compression. The transformation kinetics are modeled using a recently developed kinetic model that accounts for the stress state and the stability and size of the austenite particles. The larger austenite particles transform first and the mean volume of the austenite particles decreases with increasing strain; the decreasing austenite particle size impedes the phase transformation as the deformation proceeds. It is concluded that stress triaxiality alone cannot account for the differences in the transformation kinetics between different loading states and that the number of potential nucleation sites depends on the stress state.

## 1. Introduction

The transformation induced plasticity (TRIP)-assisted steels are a grade of low-alloyed steels that have been widely used in the automotive industry. They feature multiphase microstructures consisting of ferrite, bainite, martensite with body-centered cubic (bcc) crystal structure, and dispersed particles of metastable austenite with face-centered cubic (fcc) crystal structure. When subjected to mechanical loading, the retained austenite transforms into martensite. The shape and volume changes accompanying this transformation cause local plastic deformation in the surrounding ferrite grains, which increases the steel strength while retaining its high ductility [1,2]. The stability of austenite does not only depend on the stacking fault energy (SFE) via chemical composition and temperature [3–6], but also on the grain size [7–10], and the stress state

[11–14]. The conventional TRIP steels with polygonal ferrite are well known for their good combination of high tensile strength and high elongation [15]. However, these steels exhibit moderate bendability, flangeability and edge formability for applications that require high localized strain accommodation. Quenched and Partitioning (Q&P) steels [16] are quenched below the martensite start ( $M_s$ ) temperature and kept at the quenching temperature or reheated above the  $M_s$  temperature in order to temper the martensitic matrix. Isothermal bainitic transformation of TRIP Bainitic Ferritic (TBF) steels is undertaken above the  $M_s$  temperature, resulting in a microstructure that consists of a bainitic matrix and dispersed particles of retained austenite [17,18]. In order to avoid the presence of polygonal ferrite in the microstructure, full austenitization and a critical cooling rate are required for TBF and Q&P steels. The replacement of the polygonal ferrite matrix, as present

\* Corresponding author.

E-mail address: [efthymios.polatidis@psi.ch](mailto:efthymios.polatidis@psi.ch) (E. Polatidis).

<https://doi.org/10.1016/j.msea.2020.140321>

Received 10 April 2020; Received in revised form 7 July 2020; Accepted 21 September 2020

Available online 22 September 2020

0921-5093/© 2020 The Authors. Published by Elsevier B.V. This is an open access article under the CC BY license (<http://creativecommons.org/licenses/by/4.0/>).

in conventional TRIP steels, by bainite and/or tempered martensite, diminishes hardness differences among the respective phases. This results in outstanding edge formability and stretch-flangeability. Moreover, the metastable retained austenite particles ensure high elongations during conventional deep drawing processes [19].

The mechanical behavior of these materials is complex and macroscopic plasticity models need to account for the hardening due to plastic deformation of the phases and to incorporate kinetic models for the deformation-induced martensitic transformation [20–22]. Several transformation kinetic models have been developed. The kinetic model of Olson and Cohen [23] was the first to take into account the physical mechanisms of martensitic nucleation induced by plastic strain in austenitic steels. Olson and Cohen [23] concluded that shear band intersections are the potential nucleation sites for the formation of martensite and the rate of shear band formation is influenced by composition and temperature through the SFE. This model has been incorporated in continuum plasticity constitutive models that describe the kinetics of phase transformation and the mechanical behavior of austenitic stainless steels subjected to uniaxial tensile loading [23–26].

Recent experimental studies on austenitic steels subjected to multiaxial loading [27–29] have shown that the loading state significantly affects the TRIP effect. The combination of crystallographic texture and loading direction defines whether  $\varepsilon$ -martensite will form in low SFE steels, which is an intermediate phase for  $\alpha'$ -martensite [27] or whether deformation twins will form in medium SFE steels, which suppress the formation of  $\alpha'$ -martensite [29]. Therefore, a key element for the validation of continuum plasticity models is their ability to model the kinetics of martensite formation under multiaxial loading states which occur during operation or metal forming processes. The classical Olson-Cohen model has been modified to account for the stress state dependence of the martensitic transformation [30–32]. In most of these studies, the triaxiality factor  $\Sigma$ , defined as the ratio of the hydrostatic stress  $p$  to the von Mises equivalent stress  $\sigma_e$ , is used as a fit parameter affecting the kinetics of the martensitic transformation. The hydrostatic stress  $p$  and the von Mises equivalent stress  $\sigma_e$  are defined as

$$p = \frac{\sigma_{11} + \sigma_{22} + \sigma_{33}}{3}, \quad \sigma_e = \sqrt{\frac{3}{2} \sum_{i=1}^3 \sum_{j=1}^3 s_{ij}^2},$$

$s_{ij} = \sigma_{ij} - p\delta_{ij}$  where  $\sigma_{ij}$  and  $s_{ij}$  are the components of the stress and deviatoric stress tensors respectively and  $\delta_{ij}$  is the Kronecker delta ( $\delta_{ij} = 1$  if  $i = j$ ,  $\delta_{ij} = 0$  if  $i \neq j$ ). However, there is experimental evidence that the stress triaxiality alone cannot account completely for the dependence of phase transformation on the stress state (e.g., in 201 and 301 L austenitic steels [13,27] and in TRIP780 steel [33]). Beese et al. [13] introduced an additional stress state parameter, the Lode angle  $\theta$ , in the kinetic model of Santacreau et al. [34] to account for the complex dependence of martensite evolution on the stress state. The Lode angle  $\theta$  determines the direction of the stress deviator on the so-called “II-plane” and is defined from the relationship (e.g., Hill [35], Nayak and Zienkiewicz [36])<sup>1</sup>

$$\sin 3\theta = -\frac{27}{2} \frac{J_3}{\sigma_e^3} \quad \left( -\frac{\pi}{2} \leq 3\theta \leq \frac{\pi}{2} \right)$$

where  $J_3$  is the determinant of the stress deviator. This model was further developed to describe the deformation of TRIP-assisted steels at non-ambient temperatures by introducing a dependency of the martensitic transformation on temperature [33]. Most recently, a new

variation of the classical Olson-Cohen model was coupled with crystal plasticity to model the mechanical behavior of metastable austenitic steels under different stress states [28]. This coupled kinetic model and crystal plasticity framework accounts for i) the effect of stress state on the nucleation of martensite, ii) the evolution of the deformation texture, and iii) the SFE.

Haidemenopoulos et al. [37] developed recently a kinetic model for the martensitic transformation in TRIP-assisted steels with a relatively small fraction of metastable austenite in the form of dispersed particles in a ferrite/bainite/martensite matrix. This model describes two modes of transformation, i.e. the stress-assisted and strain-induced transformation and it is based on the modification of the nucleation site potency distribution by the applied stress and plastic strain. The model can account for the effect of austenite size, chemical composition, and stress state on the stability of austenite. It accounts for the potency of martensite nucleation in pre-existing nucleation sites (defects) or in newly created nucleation sites by deformation (formation of new defects by plasticity). The kinetic model has been applied to experimental results under uniaxial tensile loading, however, it has never been validated by experimental results under multiaxial loading (i.e. using loading states with  $\Sigma$  values other than 0.33).

In this work the kinetic model by Haidemenopoulos et al. [37] is evaluated, for the first time, under multiaxial loading in order to understand the mechanisms that control the TRIP effect under multiaxial loading. So far multiaxial loading experiments in TRIP-assisted steels have been only performed under uniaxial loading, shear, torsion or a combination of all [38,39] or punch tests [12]. The neutron diffractometer POLDI (Pulse OverLap Diffractometer) at the at Swiss spallation neutron source SINQ is equipped with a novel multiaxial loading rig which is capable of applying proportional and non-proportional biaxial loads [40,41]. In this study we report on a series of experiments undertaken for validating the kinetic model by Haidemenopoulos et al. [37] and understanding the mechanisms that control the deformation-induced phase transformations under different loading states (i.e. varying values of  $\Sigma$ ). In addition, synchrotron X-ray diffraction is performed utilizing a miniaturized multiaxial machine for quantitatively assessing the evolution of austenite size with deformation. The evolving austenite size is used as model parameter and it is seen that it affects the transformation kinetics significantly.

## 2. Materials and experiments

The material was supplied by voestalpine AG, Austria as hot-rolled sheets with a thickness of 4.35 mm. The chemical composition is given in Table 1. The mechanical response of the material upon monotonic ex situ uniaxial deformation of a dogbone sample is shown in Fig. 1.

Cruciform-shaped samples with reduced thickness at the center were designed with the aid of finite element simulations, the schematic of the cruciform is shown in Fig. 2. The special shape and the thickness reduction in the middle of the cruciform is tailored to the mechanical properties of the specific material and it is a result of a trade-off between optimizing the volume of material for sufficient neutron diffraction statistics and the possibility to reach relatively high plastic strain at the center of the cruciform prior to fracture at the cross arms.

Let  $\sigma_1$  and  $\sigma_2$  be the stresses applied macroscopically on the cruciform specimens. Three different loading combinations were tested:

- i)  $\frac{\sigma_2}{\sigma_1} = 0$  (uniaxial tension = UN),

**Table 1**

The chemical composition of the hot-rolled Q&P/TBF steel (wt.%).

C	Si	Mn	P	S	Al
0.203	1.46	2.48	0.011	0.0003	0.058

<sup>1</sup> Note that  $\theta$  is independent of the hydrostatic stress  $p$ , depends only on the stress deviator  $s$ , and takes the values:  $\theta = 30^\circ$  in uniaxial tension,  $\theta = 0^\circ$  in pure shear, and  $\theta = 30^\circ$  in uniaxial compression. Since  $s$  can be interpreted as a superposition of shears,  $\theta$  essentially characterizes the “nature” of the shear stresses at a point.

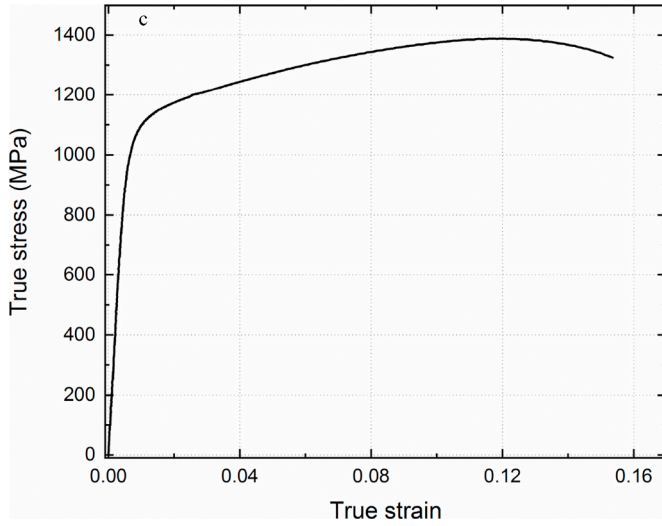


Fig. 1. Experimental true stress-strain plot for the hot-rolled Q&P/TBF steel.

- ii)  $\frac{\sigma_2}{\sigma_1} = 1$  (equibiaxial tension = EQ),
- iii)  $\frac{\sigma_2}{\sigma_1} = -\frac{1}{6}$  (biaxial tension/compression = TC).

The corresponding *macroscopic* values, i.e., the values corresponding to  $\sigma_1$  and  $\sigma_2$ , of the stress triaxiality  $\Sigma = \frac{p}{\sigma_e}$  and Lode angle  $\theta$  are.

( $\Sigma = 0.333$ ,  $\theta = -30^\circ$ ) in UN, ( $\Sigma = 0.667$ ,  $\theta = 30^\circ$ ) in EQ, ( $\Sigma = 0.254$ ,  $\theta = -22.41^\circ$ ) in TC. The triaxiality value ranges from  $-0.33$  for pure compression to  $0.667$  for equibiaxial tension. The UN, EQ and TC loading states were chosen to investigate the TRIP effect along a triaxiality range, as wide as possible, utilizing cruciform-shaped samples. It should be noted that cruciform samples are not ideal for compression tests due to buckling issues. Therefore, a moderate  $-1/6$  compression/tension loading state was chosen to avoid buckling of the sample. The  $\Sigma$  values ranging from a relatively low (TC) to an intermediate (UN) to the maximum possible (EQ) can provide significant insights into the transformation mechanisms.

The UN test was carried out using a dogbone specimen, whereas in the EQ and TC tests cruciform specimens were used. To check the actual values of ( $\Sigma$ ,  $\theta$ ) at the center of the EQ and TC specimens, where relative uniform deformations are expected to develop, we carry out detailed three-dimensional (3D) finite element calculations using the ABAQUS

general-purpose finite element program. 3D 8-node (hexahedral) elements are used with an independent interpolation for the pressure field to avoid “locking” due to the almost incompressible behavior in the plastic regime (C3D8H ABAQUS elements). A total of 52,542 elements with 233,322° of freedom (nodal displacements and element pressures) are used in the calculations. The material is modeled as isotropic elastic-plastic with Young’s modulus  $E = 205$  GPa, Poisson ratio  $\nu = 0.3$  and the von Mises plasticity criterion. The flow stress of the material is  $\sigma_0 = 738.4$  MPa and the hardening behavior is described using the data in Fig. 1. Due to the symmetries of the problem (geometry and loads), one-eighth of the entire cruciform specimen is analyzed, and symmetry conditions are imposed on the appropriate surfaces. Fig. 3 shows a “top view” of the finite element mesh used in the calculations; nine elements are used in the thickness direction (perpendicular to the mesh shown in Fig. 3).

The applied macroscopic loads  $\sigma_1$  and  $\sigma_2$  are increased proportionally from zero. The simulations show that uniform deformation is concentrated at the center of the cruciform, as shown in Fig. 3c. It is interesting to point out that the calculated values of  $\Sigma$  and  $\theta$  at the center of the specimens are different from the “macroscopic” values given above. In particular, the actual values at the center of the specimens are calculated as ( $\Sigma = 0.18$ ,  $\theta = -16^\circ$ ) for the TC loading, whereas for the EQ loading the calculated value of  $\Sigma$  agrees with the theoretical. Since the loading combination for the TC loading is close to uniaxial tension, the difference between the calculated and the macroscopic values can be attributed to the “ring” and “Poisson” effects that have been reported when cruciform specimens are loaded in uniaxial tension [41–43]. Such effects are not important when biaxial macroscopic loads are applied, and this explains the agreement between the calculated and macroscopic values for  $\Sigma$  and  $\theta$  under EQ loading. The  $\Sigma$  and  $\theta$  values remain essentially constant after the specimen deforms plastically at the cruciform center.

The in situ deformation and neutron diffraction experiments were undertaken on the POLDI instrument at the Swiss Spallation source SINQ, Switzerland, using the biaxial machine described in Refs. [40,41]. The biaxial deformation system is equipped with a 2-camera digital image correlation (DIC) system (GOM, Aramis 5 M) for measuring the in-plane macroscopic strain at the center of the cruciform, which is sprayed with a black/white pattern for tracking the displacement. The neutron diffraction measurements were carried out in load control mode after interrupting the loading at predefined force intervals and holding the displacement. The loading rate was  $40 \text{ N s}^{-1}$  for UN,  $40 \text{ N s}^{-1}$  along both axes for EQ and  $40 \text{ N s}^{-1}$  and  $-6.7 \text{ N s}^{-1}$  in tension and compression

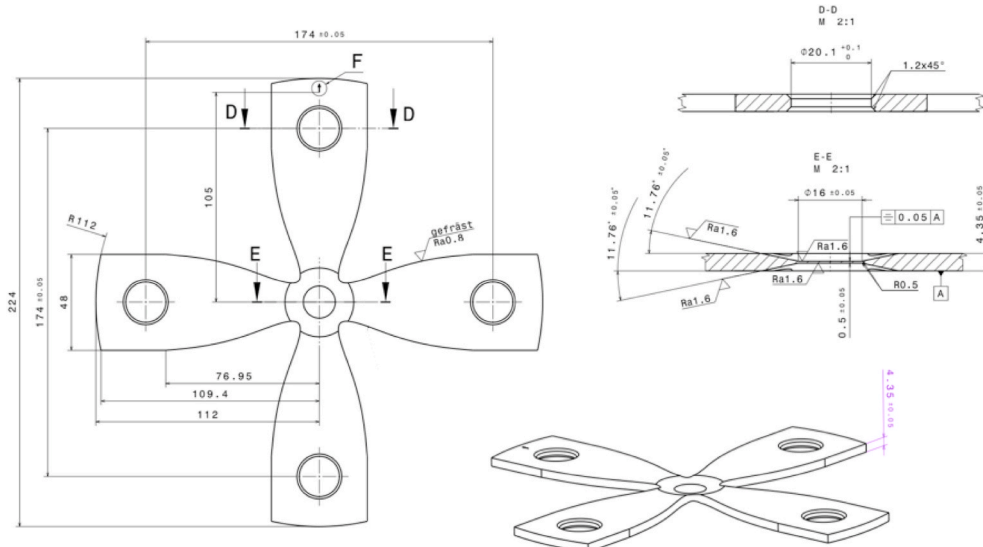
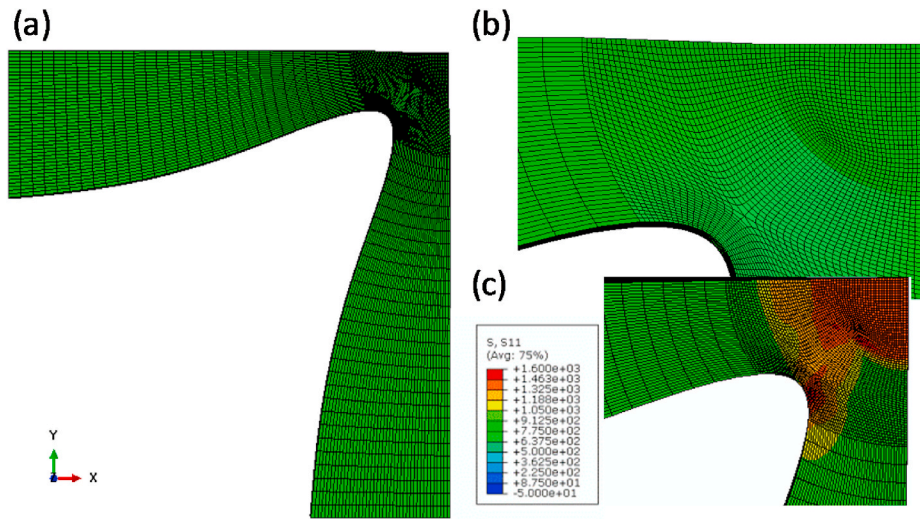


Fig. 2. Schematic of the cruciform geometry.



**Fig. 3.** Top view of the finite element mesh used in the calculations a) whole mesh, b) notch and center detail and c) uniform stress distribution at the center of the cruciform during a TC loading.

respectively for TC. Evaluating the stress state at the center of a cruciform is not as straightforward as for dogbone specimens as the cruciform samples do not have a well-defined cross-section; while experiments can only capture the applied force along each axis and strain from DIC. Hence, FE simulations are utilized for predicting the (equivalent) stress (equivalent) strain curve under EQ and TC loading as shown in Fig. 4. It is seen that the FE prediction for the TC loading, using data from UN tests, is very good since TC with a  $-1:6$  ratio is a loading state that is not significantly different than UN. However, the FE prediction is not as good as the experimental data for EQ due to mechanical anisotropy of the material along the two loading axes.

An example of neutron diffraction patterns before and after deformation is shown in Fig. 5a. The neutron diffraction data were reduced and fitted using the open-source software Mantid [44]. The obtained results were analyzed in terms of the evolution of the integrated intensity of austenite and the lower bainite/tempered martensite matrix. Since neutron diffraction cannot distinguish between the different phases with bcc crystal structures, the fitted martensite fraction corresponds to the volume fraction of deformation-induced martensite with respect to the initial volume fraction of austenite, which is calculated as

$$f_m = 1 - \frac{f_{fcc}}{f_{fcc}^0}, \quad f_{fcc}^0 = \frac{I_{fcc}^0}{I_{fcc}^0 + I_{bcc}^0}, \quad f_{fcc} = \frac{I_{fcc}}{I_{fcc} + I_{bcc}} \quad (1)$$

where  $I_{fcc}^0$  and  $I_{fcc}$  are the integrated intensities of the fcc reflections before deformation and during deformation respectively, and  $I_{bcc}^0$  and  $I_{bcc}$  are the integrated intensities of the bcc reflections before deformation and during deformation respectively. Hence,  $f_m$  varies from

0 (before loading) to 1 (when austenite transforms completely).

In situ synchrotron X-ray diffraction under equibiaxial loading was performed in transmission mode at 20 keV on the MS beamline of the Swiss Light Source using the biaxial machine described in Ref. [45]. A miniaturized cruciform sample with 250  $\mu\text{m}$  thickness in the arms and 80  $\mu\text{m}$  thickness in the center was loaded until fracture with a displacement rate of 0.1  $\mu\text{m s}^{-1}$ , while continuous diffraction measurements were undertaken. The Mythen detector of the MS station was used to record diffraction data parallel to one loading axis, a X-ray diffraction pattern is shown in Fig. 5b. The data were fitted using the open-access software WinPlotr [46]. The peak position and the full-width at half-maximum were used for assessing the evolution of the peak broadening as a function of the lattice strain. According to Williamson and Hall [47], a plot of the integral breadth  $\beta_{hkl}$  versus  $\sin(\theta_{hkl})/\lambda$ , where  $\theta_{hkl}$  is the diffraction angle and  $\lambda$  is the X-ray wavelength, produces a straight line: the intercept with the ordinate and the slope of this straight line yields values for the crystallite size and the microstrain, respectively. The intercept is inversely proportional to the crystallite size  $D$ . Due to lower resolution such investigation is not possible with the data obtained through neutron diffraction. The elastic lattice strain  $\varepsilon_{hkl}$  is determined by the relative change of the interplanar lattice spacing  $d_{hkl}$  of a specific family of planes  $\{hkl\}$  with respect to  $d_{0hkl}$ , which is the initial value prior to deformation:

$$\varepsilon_{hkl} = \frac{d_{hkl} - d_{0hkl}}{d_{0hkl}} \quad (2)$$

Electron backscatter diffraction (EBSD) was carried out on the as-received material. The sample was ground with 1200 grit SiC paper

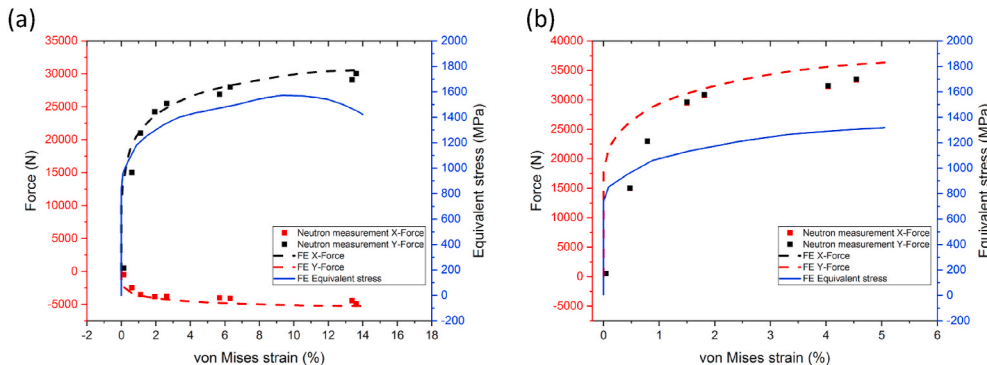


**Fig. 4.** Plots showing the applied force per axis and von Mises strain values at which neutron diffraction measurements were undertaken (black and red square symbols for x and y axis respectively). The dashed lines show the FE predictions for the applied forces per axis and von Mises strain. The blue lines are the FE predictions for the equivalent stress/von Mises strain. (a) TC and (b) EQ. (For interpretation of the references to color in this figure legend, the reader is referred to the Web version of this article.)



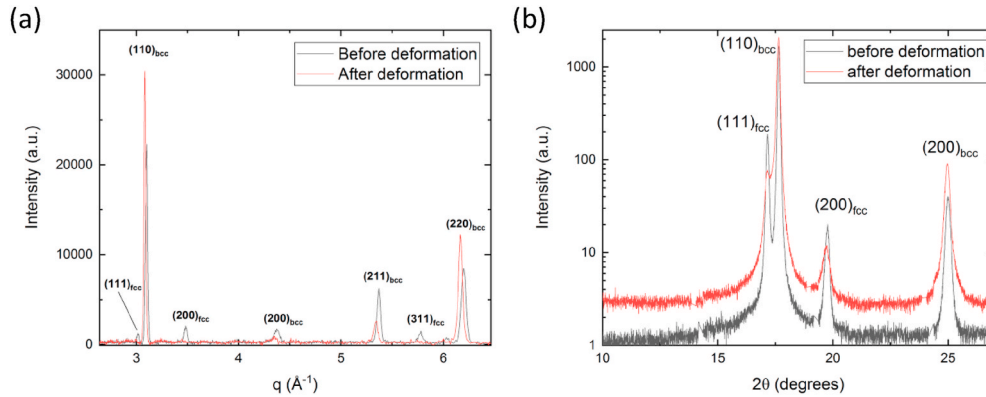


**Fig. 5.** (a) Neutron diffraction spectra before deformation and after tension/compression (6: 1 ratio) deformation at 13.8% strain. (b) synchrotron X-ray diffraction spectrum (in logarithmic scale) before and after equibiaxial loading, the  $(111)_{\text{fcc}}$  diffraction peaks does not disappear as small amount of martensite is retained after deformation.

and then electropolished for 10 s with a 16:3:1 (by volume) ethanol, glycerol, and perchloric acid solution using 52 V current. A field emission gun scanning electron microscope (FEG SEM) Zeiss ULTRA 55 equipped with EDAX Hikari Camera operated at 20 kV in high current mode with 120  $\mu\text{m}$  aperture was used. The EBSD raw data were post-processed using the commercial EDAX OIM Analysis 7.3 software.

### 3. The kinetic model

The kinetic model of Haidemenopoulos et al. [37] determines the evolution of martensite volume fraction during deformation-induced martensitic transformation of dispersed austenite particles in low-alloy TRIP-aided steels. The kinetic model is based on the Olson-Cohen [23] theory of heterogeneous nucleation of martensite, which is described by a site potency distribution function. The model thus considers that the material contains a certain number of nucleation sites from which a fraction (those with the highest potency) will transform into martensite. The model considers the effects of stress and plastic strain on the potency distribution in order to describe, respectively, the two types of martensite nucleation: i) the stress assisted (by elastic stress) and ii) the strain-induced (by plastic deformation) contributions. Additionally, the model accounts for the influence of austenite grain size and stress triaxiality on the martensitic transformation. The overall deformation-induced martensite fraction  $f_m(\varepsilon)$ , is given by:

$$f_m(\varepsilon) = 1 - \exp[-v_p N_v(\varepsilon)] \quad (3)$$

where  $\varepsilon$  is the equivalent plastic strain,  $v_p$  the mean volume of austenite particles, and  $N_v$  the number of the operational nucleation sites for martensite (i.e. the sites with sufficient potency to nucleate martensite). The term  $N_v$  consists of the operational sites under the applied stress (stress-assisted nucleation),  $N_v^\sigma$ , and the additional sites produced by plastic deformation,  $N_v^\varepsilon(\varepsilon)$ :

$$N_v(\varepsilon) = N_v^\sigma + N_v^\varepsilon(\varepsilon), \quad (4)$$

with

$$N_v^\sigma = N_v^{\sigma 0} \exp(-\alpha_\sigma n^*), \quad (5)$$

where  $N_v^{\sigma 0}$  is the number of pre-existing nucleation sites,  $\alpha_\sigma$  is a shape factor constant for the stress-modified potency distribution, and  $n^*$  is the critical embryo thickness given by:

$$n^* = -\frac{2\gamma_s}{\rho(\Delta G_{ch} + \Delta G_\sigma(\sigma) + E_{str} + W_f)}, \quad (\Delta G_{ch} < 0, \Delta G_\sigma) \quad (6)$$

where  $2\gamma_s$  is the fault/matrix interfacial energy,  $\rho$  is the density of atoms in the fault plane (in moles/unit area on a crystal plane),  $\Delta G_{ch}$  is the chemical driving force for the martensitic transformation,  $E_{str}$  is the elastic strain energy associated with the distortions in the fault interface,  $W_f$  is the frictional work of the interfacial motion. The mechanical contribution to the chemical driving force,  $\Delta G_\sigma(\sigma)$  depends on the von Mises equivalents stress  $\sigma_e$  and on the stress triaxiality  $\Sigma$ :

$$\Delta G_\sigma(p, \sigma_e) = -(0.725\sigma_e + 0.3206p) = -\sigma_e(0.725 + 0.3206\Sigma) \quad (7)$$

In isotropic materials,  $\Delta G_\sigma$  is, in general, a function of  $\sigma_e$ ,  $p$ , and  $\theta$ . In our calculations, the value of  $\sigma_e$  in Eq. (7) is taken equal to the yield stress of the material. Based on the model of Haidemenopoulos et al. [37], as the triaxiality factor increases, the critical size for martensite nucleation  $n^*$  decreases and martensite formation becomes easier. The number of operational nucleation sites upon plastic deformation  $N_v^\varepsilon(\varepsilon)$  is given by:

$$N_v^\varepsilon(\varepsilon) = N_v^{\varepsilon 0}(\varepsilon) \exp(-\alpha_\varepsilon n^*), \quad (8)$$

where  $\alpha_\varepsilon$  is a constant shape factor for the strain-modified potency distribution and  $N_v^{\varepsilon 0}$  is the additional nucleation sites produced by plastic deformation.  $N_v^{\varepsilon 0}(\varepsilon)$  given by:

$$N_v^{\varepsilon 0}(\varepsilon) = N[1 - \exp(-k\varepsilon^m)], \quad (9)$$

where  $N$  is the maximum number of nucleation sites that can be produced by plastic strain,  $k$  and  $m$  are constants.

## 4. Results

### 4.1. Crystallite size distribution

Fig. 6 shows the intercept of the Williamson-Hall (W-H) plot as a function of the lattice strain of the  $\{111\}$  lattice plane family for the in situ biaxial and synchrotron X-ray diffraction test. The evolution of the intercept of the W-H plot with deformation gives a good qualitative estimate of the relative evolution of the crystallite size. During elastic deformation, the full-width-at-half-maximum (FWHM) of the  $\{111\}$  lattice planes families is nearly constant and the W-H plot intercept remains relatively unaffected. At approximately 2250  $\mu\text{e}$  lattice strain of

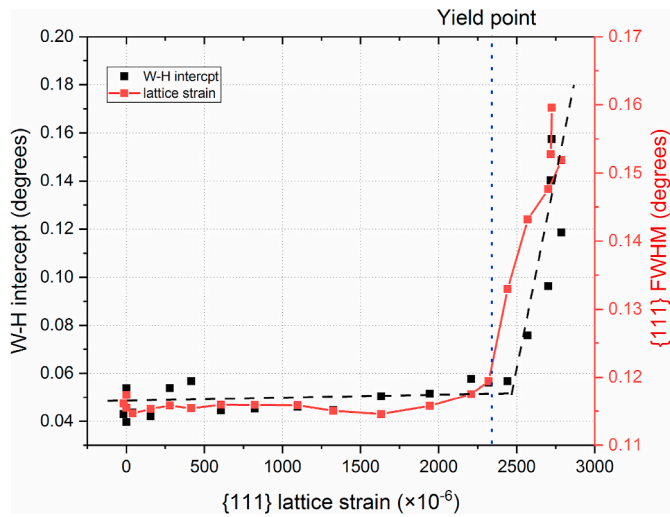


**Fig. 6.** Plot of the W–H plot intercept and the FWHM of the {111} lattice plane family as a function of the lattice strain of the {111} lattice plane family. The black dashed lines are guides for the eye. The blue dashed line indicates the point at which both FWHM and W–H intercept start to change indicating yielding of the material. (For interpretation of the references to color in this figure legend, the reader is referred to the Web version of this article.)

the {111} lattice plane family, plastic deformation takes place and the peak width starts to increase and, at the same time, the W–H plot intercept starts to increase, indicating a decrease of the mean crystallite size of austenite. By the end of the test the intercept value becomes 3 times larger, indicating a decrease of the crystallite size in the order of approximately 75%. The decreasing austenite size can be i) due to earlier transformation of the larger austenite grains, thereby reducing the average size of the ones that did not transform, ii) by the partial transformation of some austenite grains, which splits the austenite grains into smaller subgrains, or iii) by plastic deformation, which introduces intragranular misorientation within the initially (relatively) large austenite grains. A similar decrease of austenite particle size and mean crystallite size during plastic deformation under UN deformation was observed in a recent work by Haidemenopoulos et al. in a low-alloy TRIP steel with magnetic force microscopy (MFM) and X-ray diffraction (XRD) [48]. The application of the W–H plot in Ref. [48] showed that the mean crystallite size reduces by 75% after deformation, meanwhile MFM showed that the austenite grain size reduces by 50%. Based on the findings in Ref. [48] and due to the agreement of the W–H results in the current work, we assume that the austenite grain, regardless the loading state, reduces by 50% by the end of each loading test. The evolution of

the mean austenite size must be considered when using the model, since it affects the transformation kinetics. After the material fails, a small amount of austenite is still detectable (cf. Fig. 5a and b), such small fraction is beyond the detection limit of neutron diffraction.

The orientation map with inverse pole figure (IPF) coloring shown in Fig. 7 indicates a relatively mild crystallographic texture of the as-received material. The phase map of the initial microstructure consists of a lower bainite and tempered martensite matrix, both with bcc crystal structure, and dispersed austenite particles with a mean diameter of approximately 0.35  $\mu\text{m}$  and fcc crystal structure; this is in good agreement the W–H analysis, which suggests a mean crystallite size of 0.37  $\mu\text{m}$ , assuming that the grains are equiaxed and the crystallite size represents the diameter of a circle, the area of which is the same as the grain projection in 2D, in the undeformed material. Fig. 6 suggests the decreasing austenite grain size is a linear function of plastic strain, which is also confirmed in Ref. [48]. Hence, the mean austenite particle diameter, for each loading state, can be given by:

$$D_A(\epsilon_p) = D_A^0 - \frac{D_A^0}{\epsilon_{\max}} \epsilon_p \quad (10)$$

where  $D_A^0$  is the diameter of the austenite particles before deformation, i. e.,  $D_A^0 = 0.35 \mu\text{m}$ . The volume of the austenite particles  $v_p$ , is then

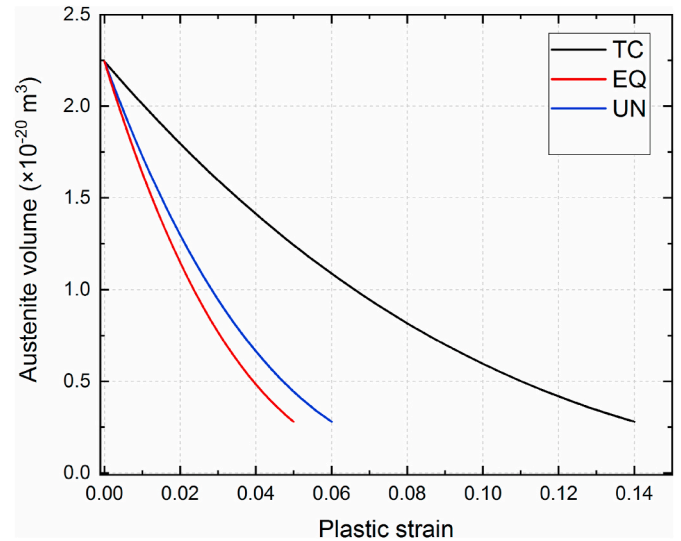


**Fig. 8.** The evolution of the mean austenite volume with plastic strain for TC, EQ and UN, used for as  $v_p$  in Eq. (3).

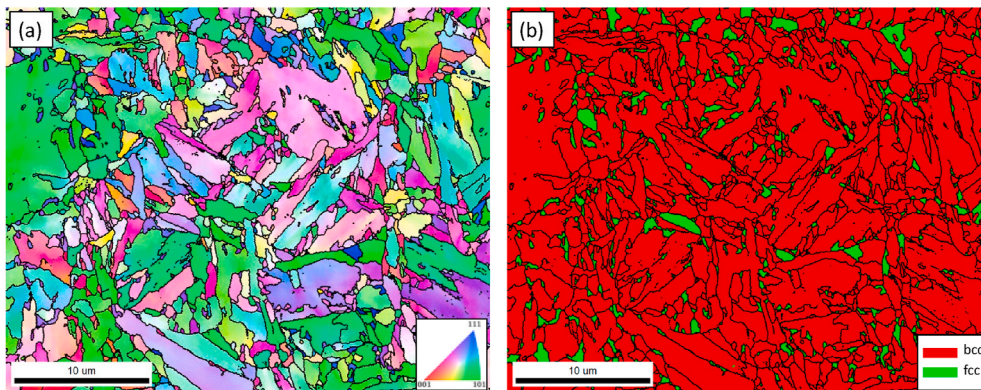


**Fig. 7.** (a) Orientation map with IPF coloring of the undeformed material in the out-of-plane direction. (b) Phase map showing the initial microstructure consisting of a bcc matrix (mixture of lower bainitic/tempered martensite) shown with red and dispersed austenite particles with fcc crystal structure shown with green. The mean austenite particle diameter is 0.35  $\mu\text{m}$ . (For interpretation of the references to color in this figure legend, the reader is referred to the Web version of this article.)

**Table 2**

The model parameters used for fitting the kinetic model to the experimental results using Eq. (3). The fitted parameters are given in **bold**.

Parameter	Value	Fitted/fixed	Common/variable	Source
$v_p$	Progresses with strain, Eq. (10)	fixed	variable	EBSD and W-H plot (present work)
$N_v^0$	<b><math>6.7 \pm 3.6 \times 10^{17} \text{ m}^{-3}</math></b>	<b>fitted</b>	<b>common</b>	<b>Fitted</b>
$n^*$	4.94, TC 4.58, EQ 4.81, UN	fixed	variable	Calculated
$\gamma_s$	0.15 J/m <sup>2</sup>	fixed	common	[37]
$\rho$	$3 \times 10^{-5} \text{ mol/m}^2$	fixed	common	[37]
$\Delta G_{ch}$	−2500 J/mol	fixed	common	[37]
$\Delta G_\sigma(\sigma)$	−770 J/mol MPa, TC −927 J/mol MPa, EQ −821 J/mol MPa, UN	fixed	variable	[37,49]
$E_{str}$	500 J/mol	fixed	common	[50]
$W_f$	745 J/mol	fixed	common	calculated from Ref. [37] based on composition
$\alpha_\sigma$	0.1	fixed	common	[37]
$N$	<b><math>1.60 \pm 1.21 \times 10^{22} \text{ m}^{-3}</math></b> , TC <b><math>1.83 \pm 1.60 \times 10^{23} \text{ m}^{-3}</math></b> , EQ <b><math>1.57 \pm 1.46 \times 10^{23} \text{ m}^{-3}</math></b> , UN	<b>fitted</b>	<b>variable</b>	<b>fitted</b>
$\alpha_\epsilon$	0.01	fixed	common	[37]
$k$	46			[37]
$m$	<b><math>2.99 \pm 0.2</math></b>	<b>fitted</b>	<b>common</b>	<b>fitted</b>

calculated by the evolution of the volume of a sphere with a diameter of  $D_A(\epsilon_p)$ . The evolution of  $v_p$  is plotted in Fig. 8 for the three loading states considered. The relationship in Eq. (10) is used in the kinetic model to describe the evolution of the mean austenite particle volume in Eq. (3).

The evolution of the deformation-induced martensite fraction with equivalent plastic strain is shown in Fig. 9 (f-ε curves). The phase transformation under TC is significantly delayed compared to the UN and EQ loadings, which exhibit similar behavior. The latter is in very good agreement with results from uniaxial and punch tests undertaken on TRIP-assisted steels by Jacques et al. [12] where it was shown that uniaxial and equibiaxial loading result in a similar evolution of martensite phase fraction.

The f-ε curves in Fig. 9 do not show a monotonic dependence on stress triaxiality,  $\Sigma$ , which is implied by the kinetic models in Ref. [30,

37]. It appears that the dependence of the phase transformation on the stress state is more complicated and may involve a strong dependence on parameters such as the different martensite nucleation mechanisms.

#### 4.2. Model fitting

The fitted kinetic model is able to describe the stress state dependence of the martensitic transformation, as shown in Fig. 9. The model was fitted to the experimental data for all three tests *simultaneously* with  $N_v^0$  and  $N$  and  $m$  as fit parameters. The possibility of  $\theta$ -dependence is not considered here; a detailed investigation of this subject is now underway. The rest of the model parameters were fixed. The fit parameters of the model are summarized in Table 2. The number of pre-existing nucleation sites,  $N_v^0$ , is a material property, which is not related to the loading state. Therefore, it was fitted and assumed to be independent of the loading state. The critical value of the embryo thickness,  $n^*$ , depends on triaxiality; therefore different  $n^*$  values were used for each loading state. The parameter  $n^*$  was calculated using Eq. (6), taking the parameter  $\Delta G_{ch}$  equal to −2500 J/mol, which is the median value used in Refs. [37]; fluctuations of  $\pm 1000$  J/mol do not affect the fit significantly. The parameter  $\Delta G_\sigma$  was set equal to −423, −510 and −451 J/mol MPa for TC, EQ, and UN respectively, based on the equation given in Ref. [37,49], using a value for  $\sigma_e = 1$  GPa, which is approximately the yield stress of the material, and the appropriate value of  $\Sigma$ . The parameter  $E_{str}$  was set to 500 J/mol from Ref. [50] and  $W_f$  was calculated using the expression given in Refs. [37], which accounts for the chemical composition of the material. The maximum number of additional nucleation sites,  $N$ , was fitted and assumed to depend on the stress state. The constants  $\alpha_\sigma$ ,  $\alpha_\epsilon$ , and  $k$  were set to the values given in Ref. [37], and  $m$  was fitted as a common constant for all loading states.

#### 5. Discussion of fitting results

Haidemenopoulos et al. [37] have demonstrated that the effect of triaxiality on the transformation kinetics is moderate, when the rest of the fitting parameters between different loading states are the same. However, the experimentally obtained evolution of the martensite fraction, in the present study, indicates that there is a stronger effect of the loading state. The obtained value for the number of pre-existing

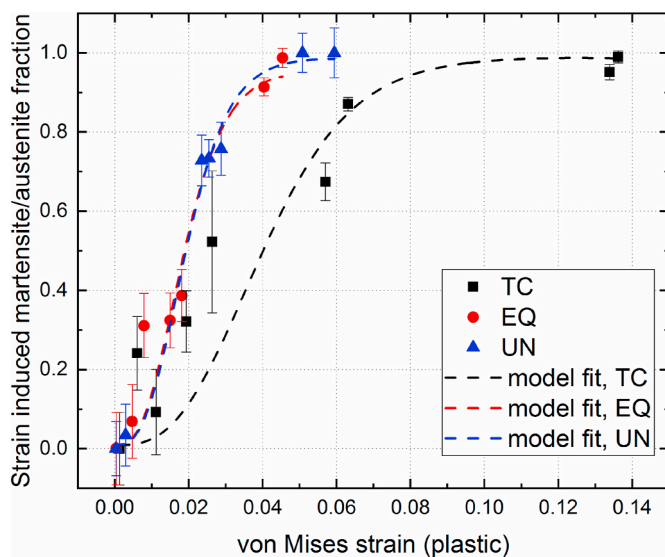


**Fig. 9.** Evolution of strain-induced martensite fraction from the retained austenite under TC, EQ, and UN loading. The dashed-lines are the fitting of the kinetic model (Eq. 3). The error bars represent the propagated uncertainty of the integrated intensity for all considered diffraction peaks in the calculation using Eq. (1).



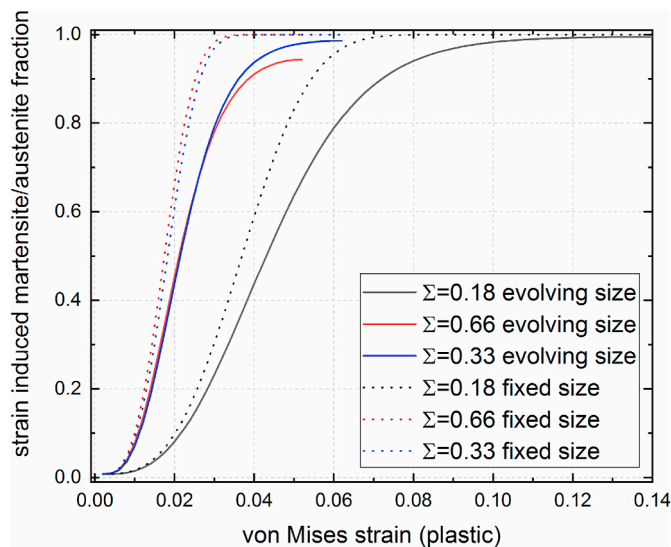


**Fig. 10.** The effect of the evolving mean volume and fixed volume ( $v_p = 2.24 \times 10^{-20} \text{ m}^3$ ) of austenite on the (modeled) transformation kinetics for the different loading states. The fit parameters are given in Table 2.

nucleation sites,  $N_v^{s0}$ , is in agreement (within the order of magnitude) with the previous fitted number of pre-existing nucleation sites under uniaxial loading state [37]. The number of additional nucleation sites that are formed by deformation is different for the different loading states, i.e., EQ loading produces slightly more nucleation sites than UN, and both significantly more than TC. This suggests that the extent of martensite formation depends strongly on the number of nucleation sites for martensite and it is less dependent on the loading state (via the triaxiality factor and hence via  $\Delta G_s$ ). This is in good agreement with previous experimental studies that show that the mechanisms of nucleation of martensite are strongly affected by the loading state, the texture of the austenite and the SFE [27,51–53].

Haidemenopoulos et al. [37] have demonstrated, in theory, the influence of austenite grain size on the stabilization of austenite and on the suppression of deformation-induced martensite. In the present study, the evolution of the mean austenite volume is considered for fitting the kinetic model to the experimental data. Fig. 10 shows the predictions of the model when the evolution of the mean austenite volume is considered (full lines) and when it is ignored (dashed lines) for the three loading states of the present study. In the latter case, a fixed value of austenite volume, i.e.  $2.24 \times 10^{-20} \text{ m}^3$  is used throughout, which is the mean volume of the austenitic particles before deformation. The plot manifests that the decreasing size of austenite particles, i.e. the increasing stability of austenite, acts as an impingement to the transformation kinetics, leading to slower saturation of the transformation and it needs to be considered when the kinetic model is applied.

There have been several studies that investigated the effect of austenite grain size on the phase stabilization, i.e. by either suppressing the TRIP effect [54] or the thermally-induced martensite formation [55–57]. The reason for the size-stabilization of austenite has been attributed to either the Hall-Petch effect that strengthens the retained austenite, thereby making it difficult to deform and hence suppressing the formation of martensite [54,58], or to the suppression of burst transformation and the autocatalytic effect by small grain size, mainly in thermally-induced martensitic transformations [59]. Therefore upon deformation, the relatively large austenite particles deform first and transform into martensite, while the smaller grains that remain austenitic resist the transformation [54].

## 6. Conclusions

Utilizing cruciform-shaped samples and in situ multiaxial deformation on the neutron diffraction instrument POLDI at SINQ, we follow the TRIP effect in a low-alloy Q&P/TBF deformed under different loading states, namely uniaxial (UN), equibiaxial (EQ), and a non-proportional tension/compression (TC) loading. The results indicate that the loading state influences the martensitic transformation; however, it does not change monotonically with triaxiality ( $\Sigma$ ) as suggested in previously developed kinetic models: TC loading exhibits the slowest martensite formation kinetics ( $\Sigma=0.18$ ), whereas UN ( $\Sigma=0.33$ ) and EQ ( $\Sigma=0.67$ ) are nearly similar. The experimental results are used for validating a recently developed kinetic model, which accounts for the effect of austenite size and stress triaxiality. It is observed that the effect of triaxiality on the transformation kinetics is moderate; however, in order to describe the observed differences, the model parameters that describe the martensite nucleation sites need to be fitted separately for different loading states. This result is confirmed by previous observations, where the martensite nucleation is dependent on the loading state. Hence, it is concluded that transformation kinetics are dictated strongly by the number of nucleation sites of martensite formation, rather than the growth of martensite (via the triaxiality factor). In situ synchrotron X-ray diffraction under biaxial loading indicates that the austenite grain size decreases with deformation; the observed evolution of austenite size is used in the kinetic model. The decreasing austenite size plays important role on the transformation kinetics, as it slows down the transformation.

## Data availability

The raw/processed data required to reproduce these findings cannot be shared at this time as the data also forms part of an ongoing study.

## CRediT authorship contribution statement

**E. Polatidis:** Conceptualization, Data curation, Formal analysis, Writing - original draft. **G.N. Haidemenopoulos:** Conceptualization, Methodology, Writing - review & editing. **D. Krizan:** Resources, Writing - review & editing. **N. Aravas:** Conceptualization, Methodology, Formal analysis, Writing - review & editing. **T. Panzner:** Investigation, Data curation, Writing - review & editing. **M. Smid:** Investigation, Writing - review & editing. **I. Papadioti:** Formal analysis. **N. Casati:** Investigation. **S. Van Petegem:** Investigation, Writing - review & editing. **H. Van Swygenhoven:** Funding acquisition, Writing - review & editing.

## Declaration of competing interest

The authors declare that they have no known competing financial interests or personal relationships that could have appeared to influence the work reported in this paper.

## Acknowledgments

EP, MS and HVS acknowledge the European Research Council for the ERC advanced Grant MULTIAx (339245). We thank Dr. R. Brönnimann (EMPA, Dübendorf) for the assistance in the mini cruciform sample preparation with the picosecond laser.

## References

- [1] P. Jacques, Q. Furnémont, A. Mertens, F. Delannay, On the sources of work hardening in multiphase steels assisted by transformation-induced plasticity, *Philos. Mag. A* 81 (2001) 1789–1812, <https://doi.org/10.1080/01418610108216637>.
- [2] P.J. Jacques, Transformation-induced plasticity for high strength formable steels, *Curr. Opin. Solid State Mater. Sci.* 8 (2004) 259–265, <https://doi.org/10.1016/j.cossms.2004.09.006>.



- [3] E.V. Pereloma, I.B. Timokhina, K.F. Russell, M.K. Miller, Characterization of clusters and ultrafine precipitates in Nb-containing C-Mn-Si steels, *Scripta Mater.* 54 (2006) 471–476, <https://doi.org/10.1016/j.scriptamat.2005.10.008>.
- [4] G.N. Haidemenopoulos, A.I. Katsamas, N. Aravas, Stability and constitutive modelling in multiphase TRIP steels, *Steel Res. Int.* 77 (2006) 720–726, <https://doi.org/10.1002/srin.200606453>.
- [5] F.G. Caballero, C. García-Mateo, J. Chao, M.J. Santofimia, C. Capdevila, C.G. de Andrés, Effects of morphology and stability of retained austenite on the ductility of TRIP-aided bainitic steels, *ISIJ Int.* 48 (2008) 1256–1262, <https://doi.org/10.2355/isijinternational.48.1256>.
- [6] R. Zhu, S. Li, I. Karaman, R. Arroyave, T. Niendorf, H.J. Maier, Multi-phase microstructure design of a low-alloy TRIP-assisted steel through a combined computational and experimental methodology, *Acta Mater.* 60 (2012) 3022–3033, <https://doi.org/10.1016/j.actamat.2012.02.007>.
- [7] R.H. Leal, J.R.C. Guimarães, Microstructure evolution during mechanically induced martensitic transformation in Fe-33%Ni-0.1%C, *Mater. Sci. Eng.* 48 (1981) 249–254, [https://doi.org/10.1016/0025-5416\(81\)90009-4](https://doi.org/10.1016/0025-5416(81)90009-4).
- [8] N.C. Goel, J.P. Chakravarty, K. Tangri, The influence of starting microstructure on the retention and mechanical stability of austenite in an intercritically annealed-low alloy dual-phase steel, *MTA 18* (1987) 5–9, <https://doi.org/10.1007/BF02646215>.
- [9] W.C. Jeong, D.K. Matlock, G. Krauss, Observation of deformation and transformation behavior of retained austenite in a 0.14C-1.2Si-1.5Mn steel with ferrite-bainite-austenite structure, *Mater. Sci. Eng., A* 165 (1993) 1–8, [https://doi.org/10.1016/0921-5093\(93\)90620-T](https://doi.org/10.1016/0921-5093(93)90620-T).
- [10] J. Hidalgo, K.O. Findley, M.J. Santofimia, Thermal and mechanical stability of retained austenite surrounded by martensite with different degrees of tempering, *Mater. Sci. Eng., A* 690 (2017) 337–347, <https://doi.org/10.1016/j.msea.2017.03.017>.
- [11] H.Y. Yu, G.Y. Kai, M. De Jian, Transformation behavior of retained austenite under different deformation modes for low alloyed TRIP-assisted steels, *Mater. Sci. Eng., A* 441 (2006) 331–335, <https://doi.org/10.1016/j.msea.2006.08.061>.
- [12] P.J. Jacques, Q. Furnémont, F. Lani, T. Pardoen, F. Delannay, Multiscale mechanics of TRIP-assisted multiphase steels: I. Characterization and mechanical testing, *Acta Mater.* 55 (2007) 3681–3693, <https://doi.org/10.1016/j.actamat.2007.02.029>.
- [13] A.M. Beese, D. Mohr, Effect of stress triaxiality and Lode angle on the kinetics of strain-induced austenite-to-martensite transformation, *Acta Mater.* 59 (2011) 2589–2600, <https://doi.org/10.1016/j.actamat.2010.12.040>.
- [14] R. Blondé, E. Jimenez-Melero, L. Zhao, N. Schell, E. Brück, S. van der Zwaag, N. H. van Dijk, The mechanical stability of retained austenite in low-alloyed TRIP steel under shear loading, *Mater. Sci. Eng., A* 594 (2014) 125–134, <https://doi.org/10.1016/j.msea.2013.11.001>.
- [15] B.C. De Cooman, Structure-properties relationship in TRIP steels containing carbide-free bainite, *Curr. Opin. Solid State Mater. Sci.* 8 (2004) 285–303, <https://doi.org/10.1016/j.cossms.2004.10.002>.
- [16] B.C.D. Cooman, J.G. Speer, Quench and partitioning steel: a new AHSS concept for automotive anti-intrusion applications, *Steel Res. Int.* 77 (2006) 634–640, <https://doi.org/10.1002/srin.200606441>.
- [17] A. Grajcar, Determination of the stability of retained austenite in TRIP-aided bainitic steel, *Journal of Achievements in Materials and Manufacturing Engineering* 20 (2007) 4.
- [18] K. Hausmann, D. Krizan, K. Spiradek-Hahn, A. Pichler, E. Werner, The influence of Nb on transformation behavior and mechanical properties of TRIP-assisted bainitic-ferritic sheet steels, *Mater. Sci. Eng., A* 588 (2013) 142–150, <https://doi.org/10.1016/j.msea.2013.08.023>.
- [19] K. Hausmann, D. Krizan, A. Pichler, E. Werner, Trip-aided Bainitic-Ferritic Sheet Steel: A Critical Assessment of Alloy Design and Heat Treatment, 2013.
- [20] M. Cherkaoui, M. Berveiller, X. Lemoine, Couplings between plasticity and martensitic phase transformation: overall behavior of polycrystalline TRIP steels, *Int. J. Plast.* 16 (2000) 1215–1241, [https://doi.org/10.1016/S0749-6419\(00\)00008-5](https://doi.org/10.1016/S0749-6419(00)00008-5).
- [21] H.N. Han, C.G. Lee, C.-S. Oh, T.-H. Lee, S.-J. Kim, A model for deformation behavior and mechanically induced martensitic transformation of metastable austenitic steel, *Acta Mater.* 52 (2004) 5203–5214, <https://doi.org/10.1016/j.actamat.2004.07.031>.
- [22] I. Papatriantafyllou, M. Agoras, N. Aravas, G. Haidemenopoulos, Constitutive modeling and finite element methods for TRIP steels, *Comput. Methods Appl. Mech. Eng.* 195 (2006) 5094–5114, <https://doi.org/10.1016/j.cma.2005.09.026>.
- [23] G.B. Olson, M. Cohen, Kinetics of strain-induced martensitic nucleation, *Metall. Mater. Trans.* 6 (1975) 791, <https://doi.org/10.1007/BF02672301>.
- [24] W.J. Dan, S.H. Li, W.G. Zhang, Z.Q. Lin, The effect of strain-induced martensitic transformation on mechanical properties of TRIP steel, *Mater. Des.* 29 (2008) 604–612, <https://doi.org/10.1016/j.matdes.2007.02.019>.
- [25] M.-G. Lee, S.-J. Kim, H.N. Han, Crystal plasticity finite element modeling of mechanically induced martensitic transformation (MIMT) in metastable austenite, *Int. J. Plast.* 26 (2010) 688–710, <https://doi.org/10.1016/j.ijplas.2009.10.001>.
- [26] H. Wang, Y. Jeong, B. Clausen, Y. Liu, R.J. McCabe, F. Barlat, C.N. Tomé, Effect of martensitic phase transformation on the behavior of 304 austenitic stainless steel under tension, *Mater. Sci. Eng., A* 649 (2016) 174–183, <https://doi.org/10.1016/j.msea.2015.09.108>.
- [27] E. Polatidis, W.-N. Hsu, M. Šmíd, T. Panzner, S. Chakrabarty, P. Pant, H. Van Swygenhoven, Suppressed martensitic transformation under biaxial loading in low stacking fault energy metastable austenitic steels, *Scripta Mater.* 147 (2018) 27–32, <https://doi.org/10.1016/j.scriptamat.2017.12.026>.
- [28] M. Zecevic, M.V. Upadhyay, E. Polatidis, T. Panzner, H. Van Swygenhoven, M. Knezevic, A crystallographic extension to the Olson-Cohen model for predicting strain path dependence of martensitic transformation, *Acta Mater.* 166 (2019) 386–401, <https://doi.org/10.1016/j.actamat.2018.12.060>.
- [29] E. Polatidis, M. Šmíd, W.-N. Hsu, M. Kubenova, J. Capek, T. Panzner, H. Van Swygenhoven, The interplay between deformation mechanisms in austenitic 304 steel during uniaxial and equibiaxial loading, *Mater. Sci. Eng., A* 764 (2019) 138222, <https://doi.org/10.1016/j.msea.2019.138222>.
- [30] R.G. Stringfellow, D.M. Parks, G.B. Olson, A constitutive model for transformation plasticity accompanying strain-induced martensitic transformations in metastable austenitic steels, *Acta Metall. Mater.* 40 (1992) 1703–1716, [https://doi.org/10.1016/0956-7151\(92\)90114-T](https://doi.org/10.1016/0956-7151(92)90114-T).
- [31] Y. Tomita, T. Iwamoto, Constitutive modeling of trip steel and its application to the improvement of mechanical properties, *Int. J. Mech. Sci.* 37 (1995) 1295–1305, [https://doi.org/10.1016/0020-7403\(95\)00039-Z](https://doi.org/10.1016/0020-7403(95)00039-Z).
- [32] M. Mansourinejad, M. Ketabchi, Modification of Olson-Cohen model for predicting stress-state dependency of martensitic transformation, *Mater. Sci. Technol.* 33 (2017) 1948–1954, <https://doi.org/10.1080/02670836.2017.1342016>.
- [33] H. Kim, J. Lee, F. Barlat, D. Kim, M.-G. Lee, Experiment and modeling to investigate the effect of stress state, strain and temperature on martensitic phase transformation in TRIP-assisted steel, *Acta Mater.* 97 (2015) 435–444, <https://doi.org/10.1016/j.actamat.2015.06.023>.
- [34] P.-O. Santacreu, J.-C. Glez, G. Chinouilh, T. Fröhlich, Behaviour model of austenitic stainless steels for automotive structural parts, *Steel Res. Int.* 77 (2006) 686–691, <https://doi.org/10.1002/srin.200606448>.
- [35] R. Hill, *The Mathematical Theory of Plasticity*, Oxford University Press, Oxford, New York, 1998.
- [36] G.C. Noyak, O.C. Zienkiewicz, Convenient form of stress invariants for plasticity, *J. Struct. Div.* 98 (1972) 949–954.
- [37] G.N. Haidemenopoulos, N. Aravas, I. Bellas, Kinetics of strain-induced transformation of dispersed austenite in low-alloy TRIP steels, *Mater. Sci. Eng., A* 615 (2014) 416–423, <https://doi.org/10.1016/j.msea.2014.07.099>.
- [38] D. Mohr, M. Oswald, A new experimental technique for the multi-axial testing of advanced high strength steel sheets, *Exp. Mech.* 48 (2008) 65–77, <https://doi.org/10.1007/s11340-007-9053-9>.
- [39] M. Dunand, D. Mohr, Ductile fracture of AHSS sheets under multi-axial loading: experiments and modeling, *AIP Conference Proceedings* 1383 (2011) 484, <https://doi.org/10.1063/1.3623648>.
- [40] J. Repper, M. Niffenegger, S. van Petegem, W. Wagner, H. van Swygenhoven, In situ biaxial mechanical testing at the neutron time-of-flight diffractometer POLDI, *Materials Science Forum*, 2014. <https://doi.org/10.4028/www.scientific.net/MSF.768-769.60>.
- [41] S. Van Petegem, J. Wagner, T. Panzner, M.V. Upadhyay, T.T.T. Trang, H. Van Swygenhoven, In-situ neutron diffraction during biaxial deformation, *Acta Mater.* 105 (2016) 404–416, <https://doi.org/10.1016/j.actamat.2015.12.015>.
- [42] V. Bonnard, J.L. Chaboche, P. Gomez, P. Kanouté, D. Pacou, Investigation of multiaxial fatigue in the context of turboengine disc applications, *Int. J. Fatig.* 33 (2011) 1006–1016, <https://doi.org/10.1016/j.ijfatigue.2010.12.018>.
- [43] R.A. Cláudio, L. Reis, M. Freitas, Biaxial high-cycle fatigue life assessment of ductile aluminium cruciform specimens, *Theor. Appl. Fract. Mech.* 73 (2014) 82–90, <https://doi.org/10.1016/j.tafmec.2014.08.007>.
- [44] O. Arnold, J.C. Bilheux, J.M. Borreguero, A. Buts, S.I. Campbell, L. Chapon, M. Doucet, N. Draper, R. Ferraz Leal, M.A. Gigg, V.E. Lynch, A. Markvardsen, D. Mikkelsen, R.L. Mikkelsen, R. Miller, K. Palmen, P. Parker, G. Passos, T. G. Perring, P.F. Peterson, S. Ren, M.A. Reuter, A.T. Savici, J.W. Taylor, R.J. Taylor, R. Tolchenov, W. Zhou, J. Zikovsky, Mantid—data analysis and visualization package for neutron scattering and  $\mu$ SR experiments, *Nucl. Instrum. Methods Phys. Res.* 764 (2014) 156–166, <https://doi.org/10.1016/j.nima.2014.07.029>.
- [45] W.-N. Hsu, E. Polatidis, M. Šmíd, S. Van Petegem, N. Casati, H. Van Swygenhoven, Deformation and degradation of superelastic NiTi under multiaxial loading, *Acta Mater.* 167 (2019) 149–158, <https://doi.org/10.1016/j.actamat.2019.01.047>.
- [46] T. Roisnel, J. Rodríguez-carvajal, WinPLOTR: a Windows tool for powder diffraction analysis, in: *Materials Science Forum. Proceedings of the European Powder Diffraction Conf, EPDIC*, 2001, 7.
- [47] G.K. Williamson, W.H. Hall, X-ray line broadening from filed aluminium and wolfram, *Acta Metall.* 1 (1953) 22–31, [https://doi.org/10.1016/0001-6160\(53\)90006-6](https://doi.org/10.1016/0001-6160(53)90006-6).
- [48] G.N. Haidemenopoulos, M. Constantinou, H. Kamoutsi, D. Krizan, I. Bellas, L. Koutsokeras, G. Constantinides, Probing the evolution of retained austenite in TRIP steel during strain-induced transformation: a multitechnique investigation, *J. Occup. Med.* 70 (2018) 924–928, <https://doi.org/10.1007/s11837-018-2832-1>.
- [49] J.R. Patel, M. Cohen, Criterion for the action of applied stress in the martensitic transformation, *Acta Metall.* 1 (1953) 531–538, [https://doi.org/10.1016/0001-6160\(53\)90083-2](https://doi.org/10.1016/0001-6160(53)90083-2).
- [50] G.N. Haidemenopoulos, M. Grujicic, G.B. Olson, M. Cohen, Transformation microyielding of retained austenite, *Acta Metall.* 37 (1989) 1677–1682, [https://doi.org/10.1016/0001-6160\(89\)90134-X](https://doi.org/10.1016/0001-6160(89)90134-X).
- [51] E. Polatidis, M. Smid, W.-N. Hsu, M. Kubenova, J. Capek, T. Panzner, H. Van Swygenhoven, The interplay between deformation mechanisms in austenitic 304 steel during uniaxial and equibiaxial loading, *Mater. Sci. Eng.* (2019) 138222, <https://doi.org/10.1016/j.msea.2019.138222>.
- [52] E. Polatidis, W.-N. Hsu, M. Šmíd, H. Van Swygenhoven, A high resolution digital image correlation study under multiaxial loading, *Exp. Mech.* 59 (2019) 309–317, <https://doi.org/10.1007/s11340-018-00443-6>.
- [53] J. Kacher, C. Kirchlechner, J. Michler, E. Polatidis, R. Schwaiger, H. V. Swygenhoven, M. Taheri, M. Legros, Impact of in situ nanomechanics on physical metallurgy, *MRS Bull.* 44 (2019) 465–470, <https://doi.org/10.1557/mrs.2019.124>.

- [54] K. Davut, S. Zaefferer, The effect of size and shape of austenite grains on the mechanical properties of a low-alloyed TRIP steel, *Steel Res. Int.* 83 (2012) 584–589, <https://doi.org/10.1002/srin.201200026>.
- [55] J. Wang, S. Van Der Zwaag, Stabilization mechanisms of retained austenite in transformation-induced plasticity steel, *Metall. Mater. Trans.* 32 (2001) 1527–1539, <https://doi.org/10.1007/s11661-001-0240-5>.
- [56] H.-S. Yang, H.K.D.H. Bhadeshia, Austenite grain size and the martensite-start temperature, *Scripta Mater.* 60 (2009) 493–495, <https://doi.org/10.1016/j.scriptamat.2008.11.043>.
- [57] S. Lee, S.-J. Lee, B.C. De Cooman, Austenite stability of ultrafine-grained transformation-induced plasticity steel with Mn partitioning, *Scripta Mater.* 65 (2011) 225–228, <https://doi.org/10.1016/j.scriptamat.2011.04.010>.
- [58] P.J. Brofman, G.S. Ansell, On the effect of fine grain size on the Ms temperature in Fe-27Ni-0.025C alloys, *MTA* 14 (1983) 1929–1931, <https://doi.org/10.1007/BF02645565>.
- [59] J.R.C. Guimarães, J.C. Gomes, A metallographic study of the influence of the austenite grain size on martensite kinetics, *Acta Metall.* 26 (1978) 1591–1596, [https://doi.org/10.1016/0001-6160\(78\)90068-8](https://doi.org/10.1016/0001-6160(78)90068-8).